

ForestLPR: LiDAR Place Recognition in Forests Attentioning Multiple BEV Density Images

Yanqing Shen^{1,2}, Turcan Tuna², Marco Hutter², Cesar Cadena², Nanning Zheng^{1*}

¹Institute of Artificial Intelligence and Robotics, Xi'an Jiaotong University

²Robotic Systems Lab, ETH Zurich

qing1159364090@stu.nnzheng@mail.xjtu.edu.cn tutuna, mahutter, cesarc@ethz.ch

Abstract

Place recognition is essential to maintain global consistency in large-scale localization systems. While research in urban environments has progressed significantly using LiDARs or cameras, applications in natural forest-like environments remain largely under-explored. Furthermore, forests present particular challenges due to high self-similarity and substantial variations in vegetation growth over time. In this work, we propose a robust LiDAR-based place recognition method for natural forests, ForestLPR. We hypothesize that a set of cross-sectional images of the forest's geometry at different heights contains the information needed to recognize revisiting a place. The cross-sectional images are represented by bird's-eye view (BEV) density images of horizontal slices of the point cloud at different heights. Our approach utilizes a visual transformer as the shared backbone to produce sets of local descriptors and introduces a multi-BEV interaction module to attend to information at different heights adaptively. It is followed by an aggregation layer that produces a rotation-invariant place descriptor. We evaluated the efficacy of our method extensively on real-world data from public benchmarks as well as robotic datasets and compared it against the state-of-the-art (SOTA) methods. The results indicate that ForestLPR has consistently good performance on all evaluations and achieves an average increase of 7.38% and 9.11% on Recall@1 over the closest competitor on intra-sequence loop closure detection and inter-sequence re-localization, respectively, validating our hypothesis¹.

1. Introduction

Place recognition in natural forest-like environments is known to be challenging due to reduced salient features and high self-similarity. Forest localization is challenging

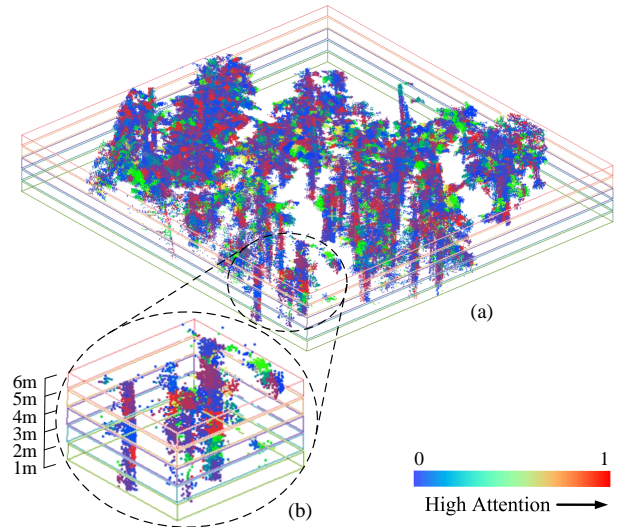


Figure 1. (a) shows a part of the point cloud submap that is colored by projected attention maps (the zoomed-in part is shown in (b)). It can be seen that after removing the ground and tree top, some canopy and bushes are still included in the cropped point cloud. Our ForestLPR framework is able to utilize multiple BEV density images and a multi-BEV interaction module to achieve adaptive attention to different heights at each patch location.

even for humans, yet it is essential for robotic navigation, simultaneous localization and mapping (SLAM), and augmented reality applications. Under poor global positioning, place recognition can provide loop-closure constraints to mitigate the adverse effects of odometry drifts in mapping applications.

Compared to the traditional registration-based methods [2], feature-based methods have become widely adopted in LiDAR place recognition, as they directly extract global features from 3D point clouds [23, 33, 51, 55] or 2D projections [13, 19, 28]. However, the primary application area of these methods is currently limited to urban environments. Few works have extended the application to forest environments [21, 37], adapting or fine-tuning the above

*Corresponding author

¹<https://github.com/shenyanqing1105/ForestLPR-CVPR2025>

learning-based models. These works have shown that a domain gap between urban and forest environments is present, and attention from the community is needed. Furthermore, the high variability within forest environments, such as tree species, age, and height, results in different point distributions. This makes it more difficult to generalize 3D models across diverse forests.

In this work, we build on two assumptions to deal with perceptual aliasing in natural forests: i) the *unique spatial distribution* and ii) the *discriminative features for different trees* can be found at different heights. In order to aid the generalization of different terrains and tree species, we discard the ground and the canopy above a given height, as those are the most affected by seasonal changes. Specifically, we crop horizontal slices at different heights, above the ground, and under the canopy, to generate a bird’s-eye view (BEV) density image of each slice. Then, we propose a multi-BEV interaction module to combine the patch-aligned features of multiple BEV images, thereby implicitly identifying stable discriminative features and achieving adaptive attention to heights at each patch location.

We compare ForestLPR with SOTA methods on Wild-Places [21], Botanic Dataset [29], and a dataset collected with a robotic platform (ANYmal Dataset). To verify the generalization ability of our method, we use the training set of Wild-Places for training and then test the other two datasets without any fine-tuning. Experimental results show that our method outperforms SOTA methods in multiple evaluations while achieving a better trade-off between performance and computational cost. Furthermore, we conduct extensive ablation studies that validate the effectiveness of using multiple BEV density images and our proposed multi-BEV interaction module.

The contributions of this paper are as follows:

- A multi-BEV interaction module that enables adaptive patch-level attention to different heights in forests, thereby mitigating information loss along the elevation axis. Our results demonstrate strong generalization across diverse forest conditions.
- An adapted Transformer-based feature extraction backbone that uses BEV density images from point clouds as input to preserve 2D geometry along the ground plane.
- A novel LiDAR-based place recognition pipeline that incorporates essential preprocessing steps to address disturbances and seasonal vegetation variations in forests.

2. Related Work

LiDAR-based place description and recognition in outdoor environments is an active field of research, typically classified into two main categories: directly utilizing 3D point clouds as input and using projected 2D images as input.

3D Point Cloud-based Methods. Recently, deep neural network based end-to-end methods [4, 12, 14, 49, 50, 54,

57, 59, 61, 62] have been developed to derive scene representations from 3D point clouds. PointNetVLAD [49] pioneered the use of an end-to-end trainable global descriptor for LiDAR place recognition, using PointNet [39] and NetVLAD [1]. However, due to the lack of spatial distribution information on local features, it is hard to directly implement PointNet in large scenes. To address this problem, LPD-Net [30] and EPC-Net [15] proposed adaptive local feature extraction and the graph-based neighborhood aggregation module. SOE-Net [54] explored the relationship between points and long-range context into local features.

More recently, many works [22, 24, 25, 55] have aimed to obtain descriptors from discretized representations of LiDAR scans. Particularly, MinkLoc3D [22] utilized sparse convolutions to capture useful point-level features. Based on MinkLoc3D, MinkLoc3Dv2 [23] proposed to combine the loss function based on a smooth approximation of the Average Precision metric. TransLoc3D [55] utilized adaptive receptive fields with a point-wise re-weighting scheme to handle objects of different sizes while suppressing noises and an external transformer to capture long-range feature dependencies. Logg3D-Net [51] proposed additional local consistency loss to guide the sparse convolutional network towards learning consistent local features across revisits. Moreover, some approaches [7, 9–11, 36, 45–47, 50] have been proposed based on segments. However, conventional segmentation methods struggle in dense forests due to the intermingling of canopy and complex tree growth.

2D Projection-based Methods. Several approaches converted 3D point clouds to 2D structures as intermediate representations and then used visual techniques to compute descriptors. 2D representations include spherical-view range images [5, 35, 43, 44], BEV bins [19], and BEV images [13, 32, 56]. For example, an interest point extractor was proposed for range images [43]. OverlapNet [5] estimated the overlap and relative yaw angle between range images based on depth, normals, and intensity values. To make the approach more accessible to generalize, OverlapTransformer [33] improved OverlapNet and created descriptors using only depth clues. However, range images are not suitable for multi-frame registered submaps.

ScanContext [19] captured height information from BEV images and integrated them into a 2D descriptor, and it was extended by using intensity [52] and semantics [27]. Still, these methods are sensitive to relative translation. ScanContext++ [20] computed Cartesian elevation maps and polar elevation maps for translational invariance. BEV image-based works treat projections as pixel-images [18, 28, 31, 58]. ContourContext [18] generated BEV projections at predefined heights, clustered the projected points, and computed the statistics from contours. However, using an elevation map as the 2D representation is sensitive to the sensor viewpoint. BVMATCH [31] used density image representa-

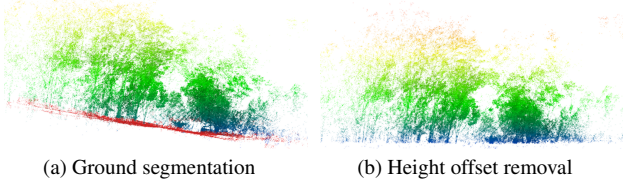


Figure 2. Results of ground segmentation and height offset removal. In (a), the ground points are marked in red. The ground segmentation result is used to remove the height offset of non-ground points, as shown in (b). Point clouds are colored by height.

tions to extract handcrafted FAST [41] key points but required training a bag-of-words model. Thus, it is not ideal for novel or unseen environments. BEVPlace [32] used group convolution [6] to extract local features and generated global features through NetVLAD [1]. MapClosures [13] proposed to extract ORB features of BEV density images.

We use BEV density images from point clouds because suitable BEV projections can preserve 2D geometry along the ground plane, which is crucial for place recognition in forests. Moreover, our solution uses multiple BEV density images generated from slices of different heights for each point cloud. It achieves adaptive attention to various heights, avoiding information loss on the elevation axis.

3. Methodology

3.1. Pre-processing of Point Cloud

The ground of natural forests can vastly vary in height, slope, and appearance. In a similar manner, the forest canopy is primarily affected by weather (e.g., wind or seasons). Thus, we pre-process the point cloud to exclude this variability by removing the height offset and removing the ground and the tree tops above a certain height.

1) *Ground Segmentation and Height Offset Removal.* We first minimally denoise the cloud and apply ground segmentation [60] to distinguish ground points from non-ground points. An example result of the ground segmentation is given in Figure 2a.

Given that tree height refers to the height of points from the ground, it is necessary to discount the ground height under a particular tree [34]. For each non-ground point \mathbf{p} , we search its *neighbor ground points*, \mathbf{p}_g , in the ground point set. The L2 distance over the x-y coordinates of \mathbf{p} and \mathbf{p}_g , $d(\mathbf{p}, \mathbf{p}_g)$, is less than a radius R . Due to the blind spots in datasets (Figure 1 in the supplementary material), some non-ground points do not have neighbor ground points in the above calculation. For these points, the radius R is gradually increased by ΔR meter until \mathbf{p} has neighbor ground points or the radius reaches a maximum radius, R_{max} . If neither condition is met, this non-ground point is removed.

For each remaining non-ground point \mathbf{p} , the average el-

evation of its neighbor ground points is subtracted from its original elevation z^p , so the final height is

$$h(\mathbf{p}) = z^p - \frac{\sum d(\mathbf{p}, \mathbf{p}_g)^{-2} z^g}{\sum d(\mathbf{p}, \mathbf{p}_g)^{-2}}, \quad (1)$$

where z^g refers to the height of \mathbf{p}_g . An example of height normalization is given in Figure 2b, converting the non-ground point cloud to a flat terrain.

2) *Ground and Tree Top Removal.* Now that all the root collars² are at the same height, we remove as many highly variable elements as possible. We give the margin of 1 m to account for terrain variations like grass, leaves, snow, and fallen branches. Similarly, we remove points above 6 m to reduce inconsistencies caused by seasonal canopy changes, as well as sparser data and occlusions due to scanning from a ground platform.

3.2. BEV Density Images from Point Cloud

To ensure robustness across different configurations of LiDAR, recent approaches [13, 31, 32] use BEV density images and have shown better performance in urban environments than other methods. Thus, we compute BEV density images from pre-processed point clouds.

1) *2D BEV Projection.* Each pre-processed point cloud is projected onto the ground plane and discretized into a 2D grid through a Cartesian BEV projection, of which the resolution is res for each cell.

The density value V of pixel (u, v) is,

$$V(u, v) = \log(V'(u, v) + 1), \quad (2)$$

where $V'(u, v)$ is the number of points in the cell. Such \log computation avoids the dominance of dense areas and preserves sparse areas during the learning process. Then, the density image is defined as,

$$I(u, v) = \frac{V(u, v) - V_{\min}}{V_{\max} - V_{\min}}, \quad (3)$$

$$V_{\max} = \max_{u, v} V(u, v); V_{\min} = \min_{u, v} V(u, v). \quad (4)$$

Such a projection preserves 2D spatial distribution.

2) *Multi-BEV Representation.* Single BEV images (create only one BEV image from the point cloud) keep the rigid structures on the 2D plane but ignore the point distribution along the z-axis, leading to information loss in the elevation direction. To address this limitation, we cut the pre-processed point cloud into S slices with a height interval of Δh . This segmentation represents a multi-layered distribution of structures.

²The point at or just above the ground level of a tree trunk.

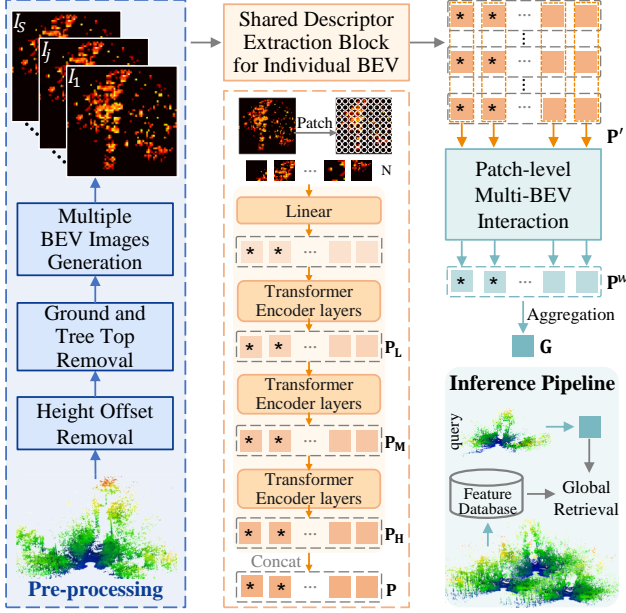


Figure 3. An overview of the proposed framework. After pre-processing, multiple BEV density images are generated from a point cloud. Each BEV image can be processed separately by the shared descriptor extraction block, combining features from multiple transformer layers. The local features are then fed into the path-level multi-BEV interaction module to highlight the discriminative features. Global descriptors are obtained through an aggregation layer. The query and database share the same pipeline to extract features during training and testing.

3.3. Descriptor Extraction Block

Here, we describe how the local features are generated from individual BEV density images, as shown in the orange dotted box in Figure 3. Given that the multi-head self-attention (MSA) operation in vision transformers [8, 48] can aggregate global contextual information, it is suitable for extracting the overall spatial distribution features.

In this work, we add an extra linear layer before the encoder of data-efficient image transformer (DeiT) [48] to match the input size. Then a BEV input tensor $I \in \mathbb{R}^{H \times W \times 1}$ is first divided into many small patches of size $p \times p$ and converted into a set of tokens $T \in \mathbb{R}^{N \times C}$ by linear projection. Here (H, W) is the resolution of the resized image, N, C denotes the number and dimension of embedding tokens, with $N = HW/p^2$. In addition to N patch tokens, DeiT adds learnable [class] and [distillation] tokens, which can be used in global descriptors.

It is observed that there are some differences in the scales of structures captured by different Transformer layers [53]. To integrate information across multiple layers, we select three groups of output patch tokens from the low-level, mid-level, and high-level layers, denoted as $\{\mathbf{P}_L, \mathbf{P}_M, \mathbf{P}_H\} \in \mathbb{R}^{(N+2) \times C}$. A group of multi-layer

patch tokens $\mathbf{P} \in \mathbb{R}^{(N+2) \times 3C}$ are firstly composed by concatenating these three groups of tokens along the channel.

3.4. Multi-BEV Interaction Module

Given that some canopy and bushes are still included in the pre-processed point cloud, we propose to perform explicit feature interaction in the z-axis to improve the generality. As shown in Figure 3, for S -slice input, each slice, I_j , is processed by the shared extraction block separately, and the set of local features is $\mathbf{P}' \in \mathbb{R}^{(N+2) \times S \times 3C}$. Then, we design a patch-level multi-BEV interaction module on features from different heights.

Specifically, we generate weight vectors for each patch to achieve adaptive attention to heights. Inspired by channel-wise attention [3], there are two considerations in designing the weighting layer: 1) Use a fixed dimension of input to make the layer compatible with different sizes of S for various applications, and 2) contain the patch-level context and capture the relative relationship in input.

For token i , we first generate $\Delta \mathbf{P}'_i \in \mathbb{R}^{S \times 3C}$,

$$\Delta \mathbf{P}'_i = \mathbf{P}'_i - \text{Mean}(\mathbf{P}'_{i,j}), \quad (5)$$

where $\Delta \mathbf{P}'_i$ represents the relative feature value. The patch-level weight vector can be generated by

$$\mathbf{w}_i = \text{SoftMax}(\Delta \mathbf{P}'_i * \mathbf{W}_a) \in \mathbb{R}^{S \times 1}, \quad (6)$$

$$\mathbf{P}_i^w = \mathbf{w}_i^T * \mathbf{P}'_i \in \mathbb{R}^{3C}, \quad (7)$$

where $\mathbf{W}_a \in \mathbb{R}^{3C \times 1}$, and $\mathbf{P}^w \in \mathbb{R}^{(N+2) \times 3C}$ consists of weighted tokens.

Global Aggregation Layer. A lightweight pooling layer, GeM [40], is applied to obtain yaw-invariant global features from patch-level local descriptors. Then, two global tokens are concatenated:

$$\mathbf{G}^* = \text{Concat}(\mathbf{P}^w[0, :], \mathbf{P}^w[1, :], \text{GeM}(\mathbf{P}^w[2, :])), \quad (8)$$

where $\mathbf{P}^w[0, :]$ and $\mathbf{P}^w[1, :]$ refer to weighted [class] and [distillation] tokens. And then the final global feature \mathbf{G} is obtained by post-processing $\mathbf{G}^* \in \mathbb{R}^{9C}$:

$$\mathbf{G} = \text{L2Norm}(\text{L2Norm}(\mathbf{G}^*) * \mathbf{W}_g), \quad (9)$$

where $\mathbf{W}_g \in \mathbb{R}^{9C \times D}$ is used for dimension reduction, D is the dimension of \mathbf{G} , and $\text{L2Norm}(\mathbf{x}) = \frac{\mathbf{x}}{\|\mathbf{x}\|}$.

Finally, we modify the DeiT by removing the classification layer and adding the proposed global aggregation layer.

3.5. Network Training

At first, we generate single BEV images from the pre-processed point cloud, and global features are computed by



Figure 4. Environment and equipment visualization of different datasets, showing diversity and richness. We use red planes to illustrate locations where the height is 1 m and yellow planes to indicate locations at a height of 6 m. It can be shown that although most of the leaves and bushes are removed, some are still included in the horizontal slices rather than having a perfectly clear appearance, which brings great challenges to methods and motivates us to use multiple BEV density images in this work.

replacing \mathbf{P}^w in Eq. (8) with \mathbf{P} . Then, the extraction block is fine-tuned on the training set of the Wild Places dataset.

After block initialization, the whole ForestLPR with multi-BEV interaction module can be further finetuned in an end-to-end fashion on the training set of Wild-Places.

In these two training steps, the commonly used triplet loss [42] is adopted to be the training objective, defined as:

$$\mathcal{L}(\mathbf{G}^q, \mathbf{G}^p, \mathbf{G}^n) = \max(d(\mathbf{G}^q, \mathbf{G}^p) - d(\mathbf{G}^q, \mathbf{G}^n) + m, 0), \quad (10)$$

where \mathbf{G}^q , \mathbf{G}^p , and \mathbf{G}^n are global features of query, positive samples, and negative samples. The margin m is a constant hyperparameter. $d(\cdot)$ refers to the Cosine distance.

Overlap-based Positive Sample Mining. Two samples are usually considered a true positive match if their distance falls below a threshold [18, 19]. It fails in object occlusion, limited field of view, and significant orientation variations [13, 26]. Due to blind spots in our benchmarks (shown in the supplementary material), it is necessary to define more realistic ground truth for training and evaluation.

We utilize volumetric overlap and use Octree to find the overlapped region. For each query and its potential positive, we use the ground truth poses to align them and voxelize them as \mathcal{V}_p and \mathcal{V}_q . The overlap can be computed as:

$$o(\mathcal{V}_q, \mathcal{V}_p) = \frac{|\mathcal{V}_q \cap \mathcal{V}_p|}{|\mathcal{V}_q \cup \mathcal{V}_p|}, \quad (11)$$

where $o(\mathcal{V}_q, \mathcal{V}_p)$ replaces the distance measure and serves as the reference for mining positives, where $o > 0.9$.

4. Implementation Details

4.1. Datasets

Wild-Places [21]. This is a challenging large-scale dataset for LiDAR place recognition in forests. It contains 8 LiDAR sequences in Venman and Karawatha and was collected using a handheld sensor payload over fourteen months. There

are different types of evaluations involving reverse revisits: *validation in training*, *intra-sequence loop closure detection*, and *inter-sequence re-localization*. The point clouds are sampled submaps with a diameter of 60 m. Following the standard dataset division of Wild-Places, we use the training/validation set of Sequences 01 and 02 for training/validation and perform intra-/inter-sequence evaluation on the defined sequences [21].

ANYmal Dataset. We collected a dataset in forests from a low perspective using the quadrupedal robot ANYmal[16, 17], equipped with a Velodyne VLP-16 scanner. For submap generation, we refer the reader to Wild-Places [21].

Botanic Dataset. Similarly, we repurpose the *Botanic-Garden* dataset [29], which is collected by Velodyne VLP-16 LiDAR. Its environment is not dense forests, allowing for more diverse testing across different scenarios.

Testing Generalization. We perform intra-sequence evaluation on ANYmal and Botanic datasets without additional fine-tuning. Figure 4 provides the visualization of benchmarks, showing high diversity. For Wild-Places, the trees are tall and dense, with few low bushes. For ANYmal, the trees are of medium height, with a lot of low vegetation. For Botanic, the trees are short and sparse.

4.2. Evaluation Metrics

Following the setting in [21], we consider a query successfully localized if the retrieved candidate is within 3 m. In addition, we use Recall@1 (R@1) and maximum F1 score (F1) as the metric for intra-sequence evaluation on all datasets, and R@1 is used for the inter-sequence assessment on Wild-Places in the paper. More details and comprehensive results are given in the supplementary material.

4.3. Training Details

Model Setting. ForestLPR is implemented using PyTorch [38]. We use DeiT-S-384 [48] as the backbone with $C = 384$. The patch size on the original image is set to 16×16 . Our extraction block contains 12 transformer encoder layers

Table 1. Benchmarking results of Intra-sequence evaluation on several standard datasets. V-03, V-04, K-03, and K-04 are subsets of Wild-Places. Bo. refers to Botanic dataset. Point-based methods are evaluated on raw point clouds. PointPillar and BEV-based methods are marked with *, showing the fine-tuning results on pre-processed point clouds and density images for fair comparison and their better performance. For TransLoc3D†, we select more suitable hyper-parameters than those in Wild-Places.

Method	V-03		V-04		K-03		K-04		ANYmal		Bo.1005-03		Bo.1005-06		Mean	
	F1	R@1														
PointPillar* [25]	28.15	37.48	73.62	62.89	41.83	39.02	77.13	70.04	50.93	41.68	65.94	70.19	70.66	62.85	58.32	54.88
TransLoc3D† [55]	22.97	35.50	75.00	64.03	43.44	38.95	75.78	75.53	49.54	38.26	71.18	76.89	76.79	68.66	59.24	56.69
MinkLoc3Dv2 [23]	49.78	49.84	82.19	71.61	51.33	50.97	80.00	71.18	72.89	66.83	29.98	43.11	31.11	34.33	56.75	55.41
LoGG3D-Net [51]	<u>53.94</u>	<u>62.40</u>	<u>80.42</u>	72.47	<u>64.30</u>	<u>64.05</u>	84.54	<u>80.26</u>	66.70	56.42	78.26	<u>79.78</u>	<u>77.88</u>	<u>82.09</u>	<u>72.29</u>	<u>71.07</u>
Scan-Context* [19]	37.66	54.80	64.49	<u>75.99</u>	34.33	50.23	66.85	63.48	<u>73.44</u>	<u>67.81</u>	34.34	49.33	60.55	76.12	53.09	62.54
BEVPlace* [32]	6.79	24.04	43.67	63.50	32.87	40.62	60.82	81.74	62.14	53.35	68.69	75.56	76.27	85.08	50.18	60.56
MapClosures* [13]	38.47	23.82	49.95	25.61	21.35	11.95	70.62	54.59	71.54	55.77	76.08	75.56	73.59	58.21	57.37	43.64
Ours	64.15	76.53	78.62	82.33	65.01	74.89	<u>81.97</u>	76.73	81.45	71.87	<u>78.21</u>	84.81	78.82	82.00	75.46	78.45

and 6 attention heads for each layer. Without loss of generality, output tokens from the second, seventh, and twelfth transformer layers are selected as \mathbf{P}_L , \mathbf{P}_M , and \mathbf{P}_H . The dimension D of final global features is set to 1024.

Training Strategy. We load the DeiT-S-384 model parameters pre-trained on ImageNet-1k³ and randomly initialize the parameters of the newly added layers. After being fine-tuned on Wild-Places, the same model is used for all evaluation experiments. $H \times W = 480 \times 480$ for training and evaluation. We apply data augmentation by randomly rotating the pre-processed point clouds around the z-axis (perpendicular to the ground) within the (π, π) interval.

Hyper-parameters. For ground filtering, we follow the standard settings of CSF⁴, except that *cloth_resolution* was changed to 0.3. For height offset removal, $R = 3$ m, $\Delta R = 1$ m, $R_{max} = 10$ m. For cropping point cloud, $S = 5$ and $\Delta h = 1$ m, where 1–6 m is used for all datasets in the experiments. The submaps are 60 m in size, and $res = 0.5$ m for BEV image generation. More details are given in the supplementary material.

5. Experimental Results

We first show the results of our approach in comparison with existing state-of-the-art methods and then analyze the effectiveness of the proposed components by ablation studies. More results are given in the supplementary material.

5.1. Comparisons with State-of-the-Art Methods

Baselines. We compare ForestLPR with previous state-of-the-art baselines, including point cloud-based methods: PointPillars [25], TransLoc3D [55], MinkLoc3Dv2 [23], and LoGG3D-Net [51], and BEV-based methods: Scan-Context [19], BEVPlace [32], and MapClosures [13]. To give a fair comparison in Table 1 and Table 2, we use BEV density images generated from the pre-processed point

cloud as the input of BEV-based methods and PointPillar, as well as re-train PointPillar and BEVPlace. We re-run the pre-trained models of TransLoc3D, MinkLoc3Dv2, and LoGG3D-Net, which are provided by Wild-places⁵. For TransLoc3D, we select more suitable hyper-parameters than those in Wild-Places [21]. (For more details and results, refer to the supplementary material.)

Intra-run Loop Closure Detection on all datasets. In this case, each submap in a sequence acts as a query to match against previously seen point clouds in the same sequence, akin to the loop-closure detection problem. According to the average ranking of methods on all datasets, LoGG3D-Net achieves the best performance among the baselines. ForestLPR shows consistently good performance, see Table 1, achieving an average increase of 7.38% on Recall@1 over SOTA performance on all datasets.

Across four evaluations of Wild-Places, ForestLPR shows an average increase of F1 and R@1 scores compared to LoGG3D-Net, 1.64% and 7.83%, respectively. Judging from the performance shown in the Table 1, V-03 and K-03 pose a greater challenge, which is because they contain a large number of reverse revisits, and in dense forests, a large portion of the environment has non-overlapping regions due to occlusion. However, ForestLPR outperforms other methods in these scenarios because it adaptively focuses on scene-specific features. For V-04 and K-04, our performance is comparable to SOTA, with only a slight decrease. For example, BEVPlace achieves SOTA on R@1 of K-04 under uniformed tree growth at the expense of the highest computational load of all tested methods.

Furthermore, ForestLPR performs well on ANYmal and Botanic datasets without fine-tuning, showing its generalization on forest scenes with various tree growth conditions. For ANYmal and Botanic datasets, differences in data collection from Wild-Places lead to different point distributions, which results in performance degradation when

³deit_small_distilled_patch16_224-649709d9.pth

⁴<https://github.com/jianboqi/CSF>

⁵<https://csiro-robotics.github.io/Wild-Places/>

Table 2. R@1 performance of Inter-sequence evaluations on Wild-Places. Inter-V/K refers to Inter-sequence evaluations, and Validation refers to the testing dataset in training. Point-based methods are evaluated on raw point clouds. PointPillar and BEV-based methods are marked with *, showing the fine-tuning results on pre-processed point clouds and density images for fair comparison and their better performance. For TransLoc3D \dagger , we use more suitable hyper-parameters than those in Wild-Places.

Method	Validation	Inter-V	Inter-K	Mean
PointPillar* [25]	35.49	60.34	52.19	49.34
TransLoc3D \dagger [55]	37.75	62.85	54.32	51.64
MinkLoc3Dv2 [23]	51.40	75.77	67.82	65.00
LoGG3D-Net [51]	<u>54.34</u>	79.84	<u>74.67</u>	<u>69.62</u>
Scan-Context* [19]	-	57.23	52.81	-
BEVPlace* [32]	26.25	51.91	41.40	39.85
MapClosures* [13]	-	34.31	19.35	-
Ours	80.03	<u>77.14</u>	79.02	78.73

the method exhibits sensitivity to point distribution variations. Compared with all methods on the ANYmal dataset, ForestLPR outperforms the SOTA method (Scan-Context) by 8.01% and 4.06% on F1 and R@1, respectively. For the Botanic dataset, ForestLPR achieves an average improvement over LoGG3D-Net of 0.45% and 2.47% on F1 and R@1, respectively.

Inter-run Re-localization on Wild-Places. For inter-sequence evaluation, like a re-localization problem, we evaluate each sequence as queries against the 3 other sequences as databases in the same environment, giving 12 evaluations per environment. Validation in Table 2 refers to the testing subset over all sequences, used for evaluating the training progress. According to the average ranking of methods on all datasets, LoGG3D-Net and MinkLoc3Dv2 achieve top 2 performance among the baselines.

In Table 2, most methods perform poorly. That’s because the sequences are collected at different times, and there are variations in tree growth. In contrast, ForestLPR, MinkLoc3Dv2, and LoGG3D-Net can achieve relatively high performance. ForestLPR achieves an average increase of 9.11% and 13.73% on Recall@1 over the top 2 performance on three inter-sequence evaluations, respectively. Specifically, since the leaves and growth of trees in the Karawatha dataset vary more across seasons than in Venman, the better performance of ForestLPR on inter-Karawatha supports its advantages in highly variable scenarios.

Computational Cost. Table 3 presents the computational cost of methods, with the implementation aligned with those in Table 1 and Table 2. All the methods are measured on Wild-Places V-04 (5,739 database submaps). For BEV-based methods, pre-processing time is fixed (30 ms), including pre-processing point cloud and BEV generation.

Except for Scan-Context and MapClosures, which re-

Table 3. Comparison of computational cost regarding feature dimension, latency, and memory footprint. All methods are measured on V-04 using the same CPU and GPU (RTX 3090). The batch size of learning-based models is 1.

Method	Latency per Query (ms) \downarrow		Memory \downarrow (MB)	Dim \downarrow
	Extraction	Retrieval		
PointPillar [25]	32.6	<u>20.2</u>	840	1024
TransLoc3D [55]	25.09	3.2	1460	256
MinkLoc3Dv2 [23]	24.74	3.2	1382	256
LoGG3D-Net [51]	64.26	<u>20.2</u>	2046	1024
Scan-Context [19]	<u>1.92</u>	384.2	-	1200
BEVPlace [32]	116.05	99.25	634	8192
MapClosures [13]	0.36	1400	-	-
ForestLPR (ours)	16.9	<u>20.2</u>	538	1024

Table 4. Ablation experiments on multiple BEV images and multi-BEV interaction module. R@1 performance is shown here.

Method	V-03	V-04	K-03	K-04	ANYmal
single BEV	53.70	64.46	54.72	70.03	58.51
concatenation	68.17	64.25	55.84	71.04	<u>63.26</u>
w/o weighting	59.68	<u>76.87</u>	63.00	71.81	58.68
w/o interaction	<u>73.76</u>	76.03	<u>67.22</u>	<u>72.23</u>	62.62
Ours	76.53	82.33	74.89	76.73	71.87

quire additional alignment, all other methods use global feature vectors for retrieval. With a descriptor size of 1024 and a retrieval time of 20.2 ms, ForestLPR has the potential to scale well to real-time robotics applications.

5.2. Ablation Studies

In this section, we validate the proposed modules.

Multiple Density Images. Without using multiple BEV images, the whole framework degenerates into generating one image from a pre-processed point cloud (*single BEV*). In Table 4, using multiple BEV images can perform better in all tests. In our experiments, tree growth in forests varies, and the pre-processed point cloud may still include some bushes and canopy rather than having a perfectly clear appearance. So the features of trees can vary at different heights, and there are occlusions and perceptual aliasing in single BEV images, which contrasts with urban scenes.

Multi-BEV Interaction Module. We conduct ablation studies on the proposed multi-BEV interaction module, mainly focusing on separate feature extraction, multi-BEV aggregation, and interaction-based weighting. Three degraded designs are as follows: 1) *Concatenation input*: multiple density images are concatenated and processed as a single unit to extract features through the modified backbone, 2) *Aggregation without weighting*: use max pooling to fuse multiple local descriptors for each patch, 3) *Weighting without interaction*: original local descriptors are used to generate weights, meaning there is no interaction between descriptors of each patch when generating weights. After

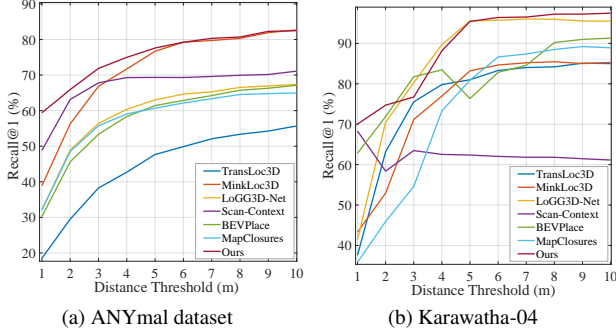


Figure 5. Recall@1 performance of methods for intra-sequence evaluations under different distance threshold. When calculating R@1, the denominator is the number of queries with corresponding positive samples, and the numerator is the number of queries that can retrieve positives. As the threshold increases, corresponding positives of one query may emerge, increasing the denominator by one and affecting monotonicity. The submap radius is 30 m.

re-training, the results are shown in Table 4.

For *concatenation*, we adjust the linear layer before the backbone to match the input size and obtain global features by placing the aggregation layer on top of the output local features. In this case, performance drops by an average of 13.96%. This suggests that feature-level interaction in the backbone is insufficient, and it is essential to pay explicit attention to each slice based on separate feature extraction. For *w/o weighting*, we use max pooling to aggregate local features for each patch. It considers different heights independently but is less effective than weighting, resulting in an average performance drop of 10.46%. For *w/o interaction*, $\Delta P_j(i)$ is replaced by $P_j(i)$ in Eq. (6). The average performance decrease of 6.10% indicates that our interaction module captures the implicit relationship between different heights more effectively than using the absolute value of features, thereby enhancing discriminative features.

5.3. Qualitative Results

During evaluation, we use 3m as the threshold to distinguish positives from the database. Here, we give the R@1 performance curves of methods under different distance thresholds in Figure 5. ForestLPR is the most accurate method at 1 m threshold, for fine localization tasks. It can also be shown that as the distance threshold increases, only ForestLPR and MinkLoc3Dv2 achieve more than 80% R@1 on the ANYmal dataset, and only ForestLPR and LoGG3D-Net achieve more than 95% R@1 on the K-04 dataset with a 10 m threshold, for other applications where a coarser localization suffices. Since the K-04 dataset is large and its retrieval space is also large, some curves in Figure 5b fluctuate, and scan-context even worsens as the threshold increases. This means that it has random matches, resulting in the proportion decline. The rising curves illustrate that most

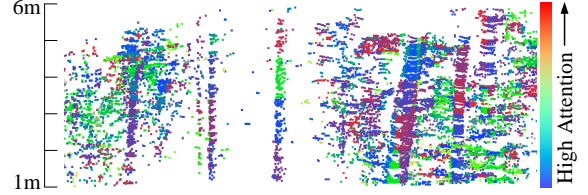


Figure 6. Front-view visualization of the point cloud with projected patch-level attention. It can be seen that different heights are given different weights, especially the trees in the middle.

so-called failure cases are in fact coming from nearby places (but beyond the threshold) and not really random matches.

As shown in Figure 6, our multi-BEV interaction module can adaptively pay attention to different heights at each patch location rather than relying only on any specific slice. The regions with the highest weights predominantly correspond to areas least affected by seasonal changes. This proves the effectiveness of our proposed interaction module and verifies our hypothesis that the geometric spatial distribution of trees and the discriminative features for different trees can be found at different heights.

6. Discussion and Conclusion

This work presents ForestLPR, a LiDAR-based place recognition method using multiple BEV density images in natural forests. The proposed approach uses a transformer-based attention mechanism to capture contextual features, which utilize the spatial distribution information of trees. Moreover, by generating multiple BEV images at different heights and introducing a multi-BEV interaction module, the proposed method can adaptively select the distinguishable features at different heights and effectively handle complex tree growth scenarios. Remarkably, it outperforms previous methods on most major forest datasets and shows generalization on datasets with different forest environments and scan patterns. Given its low computational cost, our method also has the potential to be deployed on-board robotic missions. Since our method is proposed for forests and has only been tested on forest-like datasets, it is still uncertain about its generalization to dense jungles, where it is likely that all methods would have difficulties.

Acknowledgments

This work was partly supported by the National Natural Science Foundation of China under Grants 62088102. Additionally, this work was partially supported by the EU Horizon 2020 programme grant agreement No. 101070405, the ETH Zurich Research Grant No. 21-1 ETH-27 and the Swiss National Science Foundation (SNSF) through project No. 227617. Thanks to Olga, Vaishakh, Andrei, and all my friends from ETHz RSL.

References

- [1] Relja Arandjelovic, Petr Gronat, Akihiko Torii, Tomas Pfister, and Josef Sivic. Netvlad: Cnn architecture for weakly supervised place recognition. In *CVPR*, pages 5297–5307, 2016. 2, 3
- [2] K Somani Arun, Thomas S Huang, and Steven D Blostein. Least-squares fitting of two 3-d point sets. *IEEE Transactions on pattern analysis and machine intelligence*, 9(5): 698–700, 1987. 1
- [3] Alexei A Bastidas and Hanlin Tang. Channel attention networks. In *Proceedings of the IEEE/CVF conference on computer vision and pattern recognition workshops*, pages 0–0, 2019. 4
- [4] Daniele Cattaneo, Matteo Vaghi, and Abhinav Valada. Lcdnet: Deep loop closure detection and point cloud registration for lidar slam. *IEEE Transactions on Robotics*, 38(4):2074–2093, 2022. 2
- [5] Xieyuanli Chen, Thomas Läbe, Andres Milioto, Timo Röhling, Olga Vysotska, Alexandre Haag, Jens Behley, and Cyrill Stachniss. Overlapnet: Loop closing for lidar-based slam. *arXiv preprint arXiv:2105.11344*, 2021. 2
- [6] Taco Cohen and Max Welling. Group equivariant convolutional networks. In *International conference on machine learning*, pages 2990–2999. PMLR, 2016. 3
- [7] Andrei Cramariuc, Florian Tschopp, Nikhilesh Alatur, Stefan Benz, Tillmann Falck, Marius Brühlmeier, Benjamin Hahn, Juan Nieto, and Roland Siegwart. Semssegmap–3d segment-based semantic localization. In *IEEE Int. Conf. Intell. Robots Syst.*, pages 1183–1190. IEEE, 2021. 2
- [8] Alexey Dosovitskiy, Lucas Beyer, Alexander Kolesnikov, Dirk Weissenborn, Xiaohua Zhai, Thomas Unterthiner, Mostafa Dehghani, Matthias Minderer, Georg Heigold, Sylvain Gelly, et al. An image is worth 16x16 words: Transformers for image recognition at scale. In *ICLR*, 2020. 4
- [9] Renaud Dubé, Daniel Dugas, Elena Stumm, Juan Nieto, Roland Siegwart, and Cesar Cadena. Segmatch: Segment based place recognition in 3d point clouds. In *IEEE Int. Conf. Robot. Autom.*, pages 5266–5272. IEEE, 2017. 2
- [10] Renaud Dubé, Andrei Cramariuc, Daniel Dugas, Juan Nieto, Roland Siegwart, and Cesar Cadena. SegMap: 3d segment mapping using data-driven descriptors. In *Robotics: Science and Systems (RSS)*, 2018.
- [11] Renaud Dubé, Andrei Cramariuc, Daniel Dugas, Hannes Sommer, Marcin Dymczyk, Juan Nieto, Roland Siegwart, and Cesar Cadena. Segmap: Segment-based mapping and localization using data-driven descriptors. *Int. J. Rob. Res.*, 39(2-3):339–355, 2020. 2
- [12] Zhaoxin Fan, Zhenbo Song, Hongyan Liu, Zhiwu Lu, Jun He, and Xiaoyong Du. Svt-net: Super light-weight sparse voxel transformer for large scale place recognition. In *AAAI*, pages 551–560, 2022. 2
- [13] S. Gupta, T. Guadagnino, B. Mersch, I. Vizzo, and C. Stachniss. Effectively Detecting Loop Closures using Point Cloud Density Maps. In *IEEE Int. Conf. Robot. Autom.*, 2024. 1, 2, 3, 5, 6, 7
- [14] Le Hui, Hang Yang, Mingmei Cheng, Jin Xie, and Jian Yang. Pyramid point cloud transformer for large-scale place recognition. In *ICCV*, pages 6098–6107, 2021. 2
- [15] Le Hui, Mingmei Cheng, Jin Xie, Jian Yang, and Ming-Ming Cheng. Efficient 3d point cloud feature learning for large-scale place recognition. *IEEE TIP*, 31:1258–1270, 2022. 2
- [16] Marco Hutter, Christian Gehring, Dominic Jud, Andreas Lauber, C Dario Bellicoso, Vassilios Tsounis, Jemin Hwangbo, Karen Bodie, Peter Fankhauser, Michael Bloesch, et al. Anymal-a highly mobile and dynamic quadrupedal robot. In *IEEE Int. Conf. Intell. Robots Syst.*, pages 38–44. IEEE, 2016. 5
- [17] Marco Hutter, Christian Gehring, Andreas Lauber, Fabian Gunther, Carmine Dario Bellicoso, Vassilios Tsounis, Péter Fankhauser, Remo Diethelm, Samuel Bachmann, Michael Blösch, et al. Anymal-toward legged robots for harsh environments. *Advanced Robotics*, 31(17):918–931, 2017. 5
- [18] Binqian Jiang and Shaojie Shen. Contour context: Abstract structural distribution for 3d lidar loop detection and metric pose estimation. In *IEEE Int. Conf. Robot. Autom.*, pages 8386–8392. IEEE, 2023. 2, 5
- [19] Giseop Kim and Ayoung Kim. Scan context: Egocentric spatial descriptor for place recognition within 3d point cloud map. In *IEEE Int. Conf. Intell. Robots Syst.*, pages 4802–4809. IEEE, 2018. 1, 2, 5, 6, 7
- [20] Giseop Kim, Sunwook Choi, and Ayoung Kim. Scan context++: Structural place recognition robust to rotation and lateral variations in urban environments. *IEEE Transactions on Robotics*, 38(3):1856–1874, 2021. 2
- [21] Joshua Knights, Kavisha Vidanapathirana, Milad Ramezani, Sridha Sridharan, Clinton Fookes, and Peyman Moghadam. Wild-places: A large-scale dataset for lidar place recognition in unstructured natural environments. In *IEEE Int. Conf. Robot. Autom.*, pages 11322–11328, 2023. 1, 2, 5, 6
- [22] Jacek Komorowski. Minkloc3d: Point cloud based large-scale place recognition. In *Proceedings of the IEEE/CVF Winter Conference on Applications of Computer Vision*, pages 1790–1799, 2021. 2
- [23] Jacek Komorowski. Improving point cloud based place recognition with ranking-based loss and large batch training. In *ICPR*, pages 3699–3705. IEEE, 2022. 1, 2, 6, 7
- [24] Jacek Komorowski, Monika Wyszczanska, and Tomasz Trzcinski. Egonn: Egocentric neural network for point cloud based 6dof relocalization at the city scale. *Robot. Autom. Lett.*, 7(2):722–729, 2021. 2
- [25] Alex H Lang, Sourabh Vora, Holger Caesar, Lubing Zhou, Jiong Yang, and Oscar Beijbom. Pointpillars: Fast encoders for object detection from point clouds. In *CVPR*, pages 12697–12705, 2019. 2, 6, 7
- [26] María Leyva-Vallina, Nicola Strisciuglio, and Nicolai Petkov. Data-efficient large scale place recognition with graded similarity supervision. In *CVPR*, pages 23487–23496, 2023. 5
- [27] Lin Li, Xin Kong, Xiangrui Zhao, Tianxin Huang, Wanlong Li, Feng Wen, Hongbo Zhang, and Yong Liu. Ssc: Semantic scan context for large-scale place recognition. In *IEEE Int. Conf. Intell. Robots Syst.*, pages 2092–2099. IEEE, 2021. 2
- [28] Yanhao Li and Hao Li. Lidar-based initial global localization using two-dimensional (2d) submap projection image (spi).

- In *IEEE Int. Conf. Robot. Autom.*, pages 5063–5068, 2021. 1, 2
- [29] Yuanzhi Liu, Yujia Fu, Minghui Qin, Yufeng Xu, Baoxin Xu, Fengdong Chen, Bart Goossens, Poly Z.H. Sun, Hongwei Yu, Chun Liu, Long Chen, Wei Tao, and Hui Zhao. Botanicgarden: A high-quality dataset for robot navigation in unstructured natural environments. *Robot. Autom. lett.*, 9(3): 2798–2805, 2024. 2, 5
- [30] Zhe Liu, Shunbo Zhou, Chuanzhe Suo, Peng Yin, Wen Chen, Hesheng Wang, Haoang Li, and Yun-Hui Liu. Lpd-net: 3d point cloud learning for large-scale place recognition and environment analysis. In *ICCV*, pages 2831–2840, 2019. 2
- [31] Lun Luo, Si-Yuan Cao, Bin Han, Hui-Liang Shen, and Junwei Li. Bvmatch: Lidar-based place recognition using bird’s-eye view images. *Robot. Autom. lett.*, 6(3):6076–6083, 2021. 2, 3
- [32] Lun Luo, Shuhang Zheng, Yixuan Li, Yongzhi Fan, Beinan Yu, Si-Yuan Cao, Junwei Li, and Hui-Liang Shen. Bevplace: Learning lidar-based place recognition using bird’s eye view images. In *ICCV*, pages 8700–8709, 2023. 2, 3, 6, 7
- [33] Junyi Ma, Jun Zhang, Jintao Xu, Rui Ai, Weihao Gu, and Xieyuanli Chen. Overlaptransformer: An efficient and yaw-angle-invariant transformer network for lidar-based place recognition. *Robot. Autom. lett.*, 7(3):6958–6965, 2022. 1, 2
- [34] M.V.R. Malladi, T. Guadagnino, L. Lobefaro, M. Mattamala, H. Griess, J. Schweier, N. Chebrolu, M. Fallon, J. Behley, and C. Stachniss. Tree Instance Segmentation and Traits Estimation for Forestry Environments Exploiting LiDAR Data Collected by Mobile Robots. In *IEEE Int. Conf. Robot. Autom.*, 2024. 3
- [35] A. Milioto, I. Vizzo, J. Behley, and C. Stachniss. RangeNet++: Fast and Accurate LiDAR Semantic Segmentation. In *IEEE Int. Conf. Intell. Robots Syst.*, 2019. 2
- [36] Guilherme V Nardari, Avraham Cohen, Steven W Chen, Xu Liu, Vaibhav Arcot, Roseli AF Romero, and Vijay Kumar. Place recognition in forests with urquhart tessellations. *Robot. Autom. lett.*, 6(2):279–286, 2020. 2
- [37] Haedam Oh, Nived Chebrolu, Matias Mattamala, Leonard Freißmuth, and Maurice Fallon. Evaluation and deployment of lidar-based place recognition in dense forests. *arXiv preprint arXiv:2403.14326*, 2024. 1
- [38] Adam Paszke, Sam Gross, Francisco Massa, Adam Lerer, James Bradbury, Gregory Chanan, Trevor Killeen, Zeming Lin, Natalia Gimelshein, Luca Antiga, et al. Pytorch: An imperative style, high-performance deep learning library. *NeurIPS*, 32, 2019. 5
- [39] Charles R Qi, Hao Su, Kaichun Mo, and Leonidas J Guibas. Pointnet: Deep learning on point sets for 3d classification and segmentation. In *CVPR*, pages 652–660, 2017. 2
- [40] Filip Radenović, Giorgos Tolias, and Ondřej Chum. Fine-tuning cnn image retrieval with no human annotation. *IEEE TPAMI*, 41(7):1655–1668, 2018. 4
- [41] Edward Rosten and Tom Drummond. Machine learning for high-speed corner detection. In *ECCV*, pages 430–443. Springer, 2006. 3
- [42] Florian Schroff, Dmitry Kalenichenko, and James Philbin. Facenet: A unified embedding for face recognition and clustering. In *CVPR*, pages 815–823, 2015. 5
- [43] Bastian Steder, Giorgio Grisetti, and Wolfram Burgard. Robust place recognition for 3d range data based on point features. In *IEEE Int. Conf. Robot. Autom.*, pages 1400–1405. IEEE, 2010. 2
- [44] Bastian Steder, Michael Ruhnke, Slawomir Grzonka, and Wolfram Burgard. Place recognition in 3d scans using a combination of bag of words and point feature based relative pose estimation. In *IEEE Int. Conf. Intell. Robots Syst.*, pages 1249–1255. IEEE, 2011. 2
- [45] Georgi Tinchev, Simona Nobili, and Maurice Fallon. Seeing the wood for the trees: Reliable localization in urban and natural environments. In *IEEE Int. Conf. Intell. Robots Syst.*, pages 8239–8246. IEEE, 2018. 2
- [46] Georgi Tinchev, Adrian Penate-Sanchez, and Maurice Fallon. Learning to see the wood for the trees: Deep laser localization in urban and natural environments on a cpu. *Robot. Autom. lett.*, 4(2):1327–1334, 2019.
- [47] Georgi Tinchev, Adrian Penate-Sanchez, and Maurice Fallon. Real-time lidar localization in natural and urban environments. *arXiv preprint arXiv:2301.13583*, 2023. 2
- [48] Hugo Touvron, Matthieu Cord, Matthijs Douze, Francisco Massa, Alexandre Sablayrolles, and Herve Jegou. Training data-efficient image transformers & distillation through attention. In *International Conference on Machine Learning*, pages 10347–10357, 2021. 4, 5
- [49] Mikaela Angelina Uy and Gim Hee Lee. Pointnetvlad: Deep point cloud based retrieval for large-scale place recognition. In *CVPR*, pages 4470–4479, 2018. 2
- [50] Kavisha Vidanapathirana, Peyman Moghadam, Ben Harwood, Muming Zhao, Sridha Sridharan, and Clinton Fookes. Locus: Lidar-based place recognition using spatiotemporal higher-order pooling. In *IEEE Int. Conf. Robot. Autom.*, pages 5075–5081, 2021. 2
- [51] Kavisha Vidanapathirana, Milad Ramezani, Peyman Moghadam, Sridha Sridharan, and Clinton Fookes. Logg3d-net: Locally guided global descriptor learning for 3d place recognition. In *IEEE Int. Conf. Robot. Autom.*, pages 2215–2221. IEEE, 2022. 1, 2, 6, 7
- [52] Han Wang, Chen Wang, and Lihua Xie. Intensity scan context: Coding intensity and geometry relations for loop closure detection. In *IEEE Int. Conf. Robot. Autom.*, pages 2095–2101. IEEE, 2020. 2
- [53] Ruotong Wang, Yanqing Shen, Weiliang Zuo, Sanping Zhou, and Nanning Zheng. Transvpr: Transformer-based place recognition with multi-level attention aggregation. In *CVPR*, pages 13648–13657, 2022. 4
- [54] Y. Xia, Y. Xu, S. Li, R. Wang, J. Du, D. Cremers, and U. Stilla. Soe-net: A self-attention and orientation encoding network for point cloud based place recognition. In *CVPR*, 2021. 2
- [55] Tian-Xing Xu, Yuan-Chen Guo, Zhiqiang Li, Ge Yu, Yu-Kun Lai, and Song-Hai Zhang. Transloc3d: Point cloud based large-scale place recognition using adaptive receptive fields. *arXiv preprint arXiv:2105.11605*, 2021. 1, 2, 6, 7
- [56] Xuecheng Xu, Sha Lu, Jun Wu, Haojian Lu, Qiuguo Zhu, Yiyi Liao, Rong Xiong, and Yue Wang. Ring++: Rotation-invariant gram for global localization on a sparse scan map. *IEEE Transactions on Robotics*, 2023. 2

- [57] Bochun Yang, Zijun Li, Wen Li, Zhipeng Cai, Chenglu Wen, Yu Zang, Matthias Muller, and Cheng Wang. Lisa: Lidar localization with semantic awareness. In *CVPR*, pages 15271–15280, 2024. [2](#)
- [58] Chongjian Yuan, Jiarong Lin, Zuhao Zou, Xiaoping Hong, and Fu Zhang. Std: Stable triangle descriptor for 3d place recognition. In *IEEE Int. Conf. Robot. Autom.*, pages 1897–1903. IEEE, 2023. [2](#)
- [59] Wenxiao Zhang and Chunxia Xiao. Pcan: 3d attention map learning using contextual information for point cloud based retrieval. In *CVPR*, pages 12436–12445, 2019. [2](#)
- [60] Wuming Zhang, Jianbo Qi, Peng Wan, Hongtao Wang, Donghui Xie, Xiaoyan Wang, and Guangjian Yan. An easy-to-use airborne lidar data filtering method based on cloth simulation. *Remote sensing*, 8(6):501, 2016. [3](#)
- [61] Jiawei Zhou, Ruben Mascaro, Cesar Cadena, Margarita Chli, and Lucas Teixeira. Temporal- and viewpoint-invariant registration for under-canopy footage using deep-learning-based bird’s-eye view prediction. In *IEEE Int. Conf. Intell. Robots Syst.* IEEE, 2024. [2](#)
- [62] Zhicheng Zhou, Cheng Zhao, Daniel Adolphsson, Songzhi Su, Yang Gao, Tom Duckett, and Li Sun. Ndt-transformer: Large-scale 3d point cloud localisation using the normal distribution transform representation. In *IEEE Int. Conf. Robot. Autom.*, pages 5654–5660. IEEE, 2021. [2](#)